applied sciences

MDPI

Article

Fatigue Behavior of Prestressed Concrete Beam for Straddle-Type Monorail Tracks

Qianhui Pu [1], Hanyu Wang [1], Hongye Gou [1,2,*], Yi Bao [3] and Meng Yan [4]

[1] Department of Bridge Engineering, School of Civil Engineering, Southwest Jiaotong University, Chengdu 610031, China; qhpu@vip.163.com (Q.P.); im.why@hotmail.com (H.W.)
[2] Key Laboratory of High-speed Railway Engineering of the Ministry of Education, Southwest Jiaotong University, 111 Section of the Northbound 1, Second Ring Rd., Chengdu 610031, China
[3] Department of Civil and Environmental Engineering, University of Michigan, 500 S State St, Ann Arbor, MI 48109, USA; ybc86@mst.edu
[4] Sichuan Jiaoda Inspection and Consulting Engineering Company Limited, Chengdu 610031, China; yanmeng@jdjc.net
* Correspondence: gouhongye@home.swjtu.edu.cn; Tel.: +86-159-8238-9062

Received: 24 June 2018; Accepted: 9 July 2018; Published: 13 July 2018

Abstract: Monorail transportation systems are widely built in medium and small cities, as well as hilly cities, because of their excellent performance. A prestressed concrete track beam is a key load-carrying structural component and guideway subjected to repeated traffic load. The fatigue behavior of the prestressed concrete beam is critical for the safety of the transportation system. This paper presents the results of an experimental study on the fatigue behavior of a prestressed concrete beam in terms of stiffness degradation and strain change. The displacement and rotation of the beam of concrete and reinforcement were examined, respectively. A three-dimensional finite element model was established to help understand the development of the mechanical behavior. No crack was observed throughout the test. Both concrete and bars behaved in their linear-elastic stage throughout the test, and the bond between them performed well.

Keywords: straddle-type monorail transportation; prestressed concrete beam; model test; fatigue; stiffness degradation

1. Introduction

With the fast expansion of modern cities, different types of urban rail transit systems have been developed to address the increasing challenge of traffic congestion [1]. Monorail transportation systems have been widely used in medium and small cities as well as hilly cities [2,3] owing to their excellent climbing ability, lower noise, and shorter construction period [4]. Monorail transportation systems can be classified into two categories: (1) straddle types, and (2) suspension types [5], according to how the monorail vehicle is operated. The track beam of a suspension type system is mainly made of steel, which is costly and requires frequent maintenance.

As a critical component of straddle-type monorail systems [6], prestressed concrete (PC) track beams serve as the load-bearing structure and guideway subjected to repeated traffic load, influencing the safety of transportation infrastructure. Under such circumstances, the fatigue effect on mechanical behavior generally results in the degradation of stiffness and load-bearing capacity, having adverse effects in the comfort of passengers [7]. This consideration is particularly important for monorail track beams due to the large proportion of live load (more than 50%). Fatigue behavior must be considered in design to satisfy the safety and serviceability requirements [8,9].

During the last decade, a large amount of theoretical and experimental research has been proposed to investigate the fatigue behavior and mechanism of the PC beam in detail [10–12]. Harajli and Naaman [13] found that the fatigue life of PC beams is related to the degree of prestressing, the longitudinal reinforcement ratio, and the strength of concrete. Feng et al. [14] found that cracking and deflection changed rapidly in the initial stage of fatigue, and changed stably afterwards until failure. Wollmann [15] carried out an experimental investigation of the fatigue strength of post-tensioned concrete girders, finding that fatigue failure occurred in the vicinity of cracks. Li et al. [16] analyzed the evolution of the fatigue failure pattern of PC beams and regularities of midspan deflection and strain of concrete of PC beams. However, most of the studies focused on the fatigue behavior of partially-prestressed concrete beams [17] and beams strengthened with carbon fiber-reinforced plastics sheets [18–21]. However, there is no research on fatigue behavior of fully prestressed concrete beams. The primary reason is that fully prestressed concrete beams are considered not susceptible to fatigue damage due to the applied full prestressing force. However, fully prestressed concrete beams can be turned into partially prestressed concrete beams under the effects of overloading or other extreme events. Moreover, cracks are not allowed in fully prestressed concrete beams under service loads, which is different from partially prestressed concrete beams.

Model tests and in situ tests have been considered as effective approaches to investigate mechanical performances of structures [22–30]. In this study, a full-scale fatigue test of a prestressed concrete beam was carried out. Displacement, rotation, strain of concrete, and reinforcement were examined under post-fatigue static loading condition. A three-dimensional finite element model was established to understand stress distributions.

2. Experimental Program

2.1. Materials

A PC beam was fabricated to represent the typical PC track beam for a straddle-type monorail. The cube compressive strength, tensile strength, and elastic modulus of the concrete were 60 MPa, 3.5 MPa, and 41 GPa, respectively. The reinforcement bars were HRB400, providing yield strength and elastic modulus of 400 MPa and 200 GPa, respectively. The yield strength and elastic modulus of prestressed tendons were 1860 MPa and 195 GPa.

2.2. Test Models

The PC beam had a rectangular hollow cross section measuring 700 mm (width) × 1500 mm (height) and a length of 24,000 mm (net span 23,200 mm). The end of the girder specimen had a solid section to accommodate the application of the post-tensioning force. The detailed dimensions are shown in Figure 1.

As laid out in Figure 2, the internal reinforcements were threaded bars with diameters of 16 mm and 12 mm, which were classified into six categories. The diameter and length of each category are listed in Table 1. N3 and N6 were longitudinally distributed in the top and bottom plates and webs, while N1, N4, and N5 were stirrups and N2 were transverse bars for the stability of the stirrups.

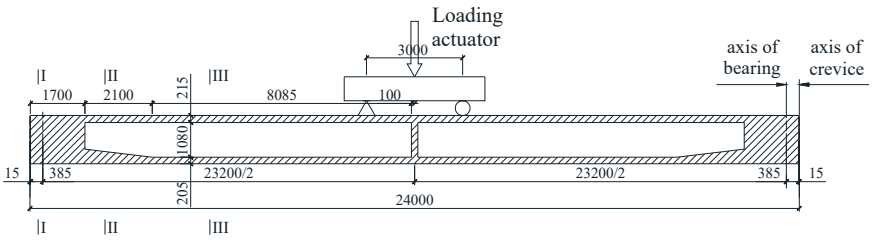

(**a**)

Figure 1. *Cont.*

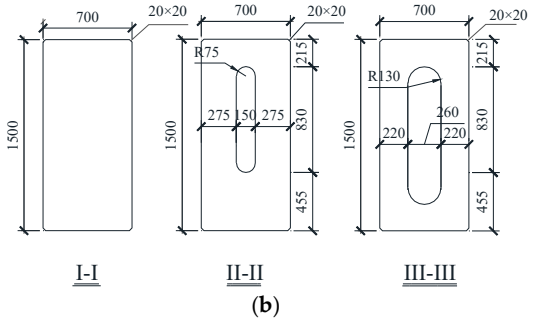

Figure 1. Detailed dimensions of the specimen (unit: mm): (**a**) Front of elevation; (**b**) sectional view.

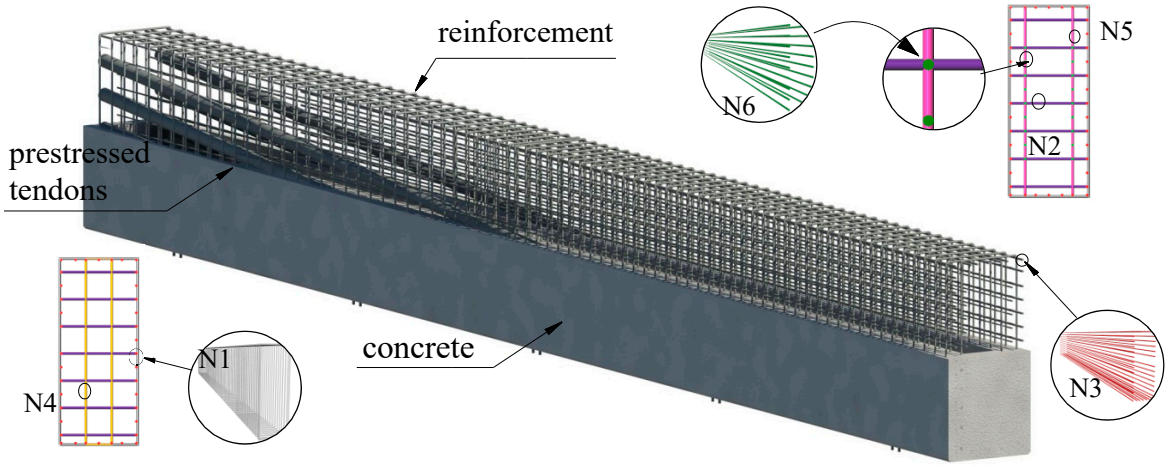

Figure 2. Details of reinforcement bars.

Table 1. Mechanical properties of reinforcement steel.

Identifier	N1	N2	N3	N4	N5	N6
Diameter (mm)	C16	C16	C16	C12	C12	C12
Length of Each (mm)	4414	994	23,890	3674	3784	23,892
Number	142	516	40	58	82	18

The prestressed tendons were tensioned when the concrete age exceeded 28 days. Prestressing is mainly controlled by the digital reading of the jack placed on the anchor, and the elongation is used for checking. The stretching control stress was 1361 MPa, and the elongation is shown in Table 2. The geometric dimensions are shown in Figure 3 and the values of the parameters are shown in Table 3.

Table 2. Details of prestressing the tendons.

Tendon	Specification	Control Stress for Prestressing (MPa)	Elongation (mm)		Tensioning Arrangement
			Left	Right	
P1	7-7ϕ5	1361	78.8	78.8	4
P2	7-7ϕ5	1361	78.7	78.7	2
P3	7-7ϕ5	1361	78.5	78.5	5
P4	4-7ϕ5	1361	78.2	78.2	1
P5	3-7ϕ5	1361	78.0	78.0	3

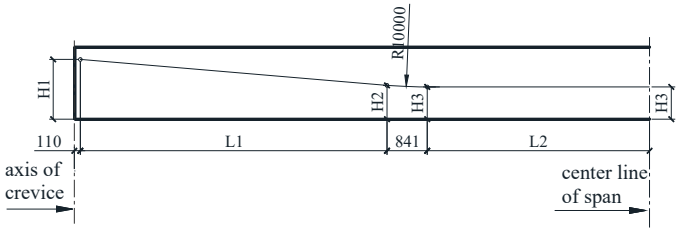

Figure 3. Geometric dimensions of prestressed tendons (unit: mm).

Table 3. Geometric parameter of prestressed tendons (unit: mm).

Tendon	H1	H2	H3	L1	L2
P1	1245	705	670	6395	4639
P2	995	595	530	5092	5943
P3	745	425	390	3788	7246
P4	495	285	250	2484	8550
P5	245	145	110	1180	9854

2.3. Test Setup

The loading tests were conducted in the Structures Laboratory at Southwest Jiaotong University. The load was applied with a Material Testing System (MTS) electrohydraulic servo actuator (Eaton Corporation Automation Products Division, Troy, MI, USA), while the loading point at midspan was divided into two points as shown in Figure 1. The test setup and the loading site are shown in Figures 4 and 5, respectively.

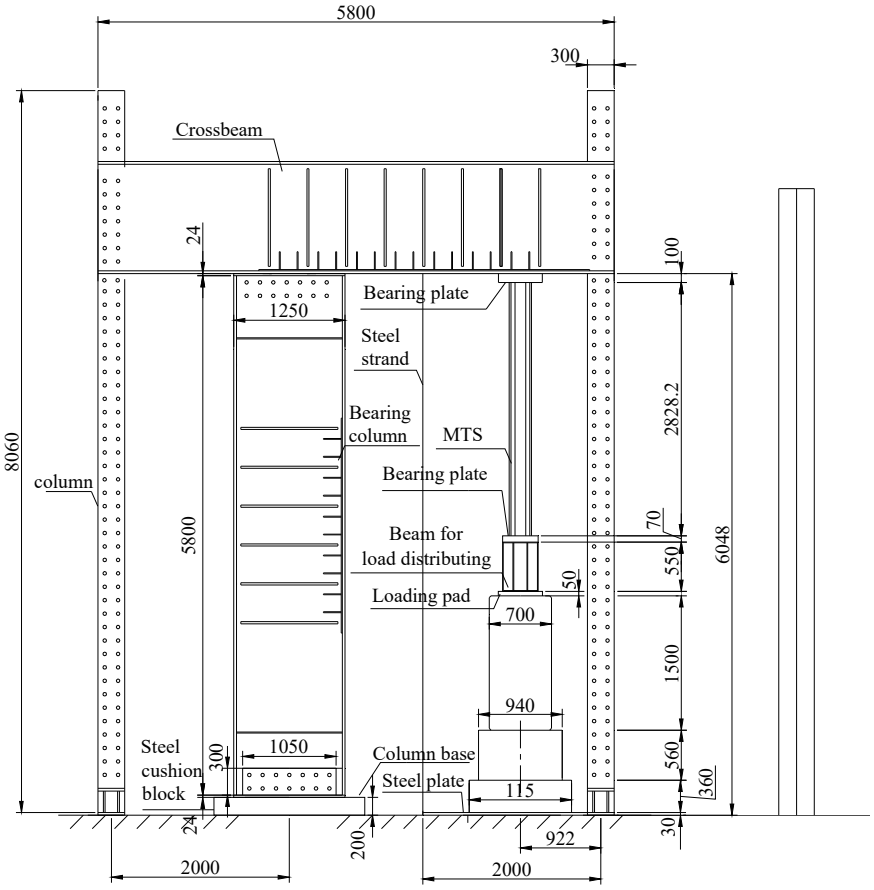

Figure 4. Elevation schematic view of the test setup (unit: mm).

(**a**) (**b**)

Figure 5. Loading setup: (**a**) specimen and device; (**b**) detail of Material Testing System (MTS) electrohydraulic servo actuator.

2.4. Instrumentation

(1) Displacement Measurement: For obtaining the degradation of the beam's stiffness, the deflection at cross sections A-A, C-C, and E-E were measured using dial gauges with a measurement range of ±50 mm and a precision of 0.01 mm. To balance the settlement caused by the supports, dial gauges were placed at the supports. There were two deflection measurement points at each section, totaling 10 over the beam. The schematic of the deflection test is shown in Figure 6a, represented in blue.

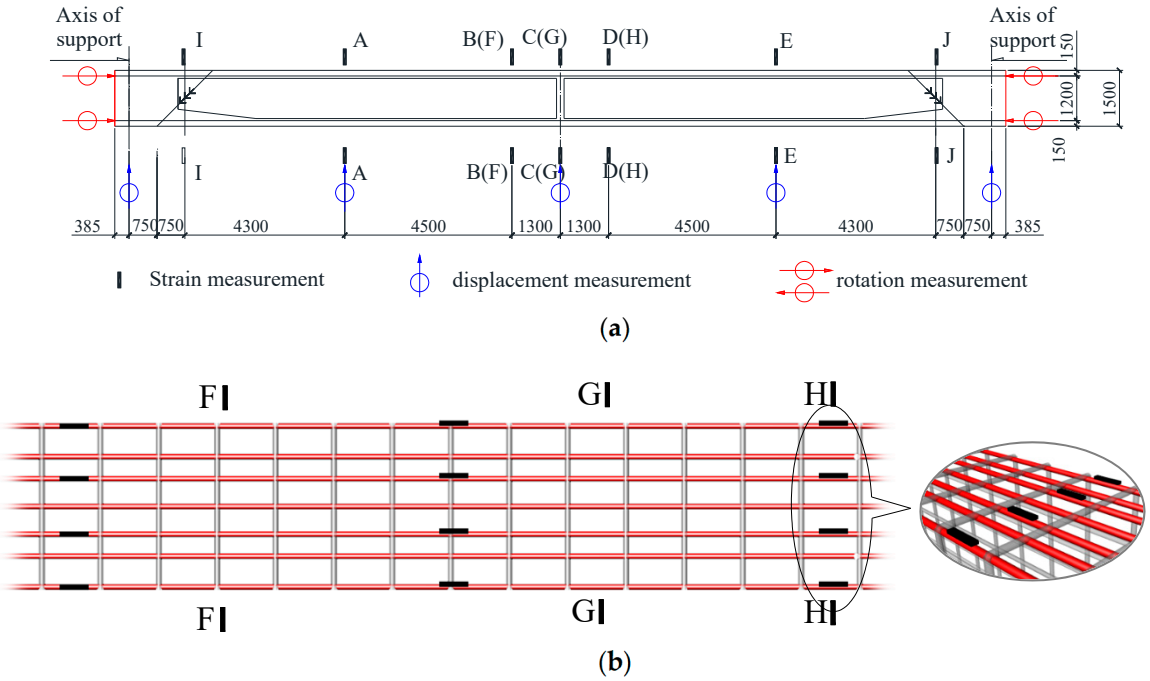

Figure 6. *Cont.*

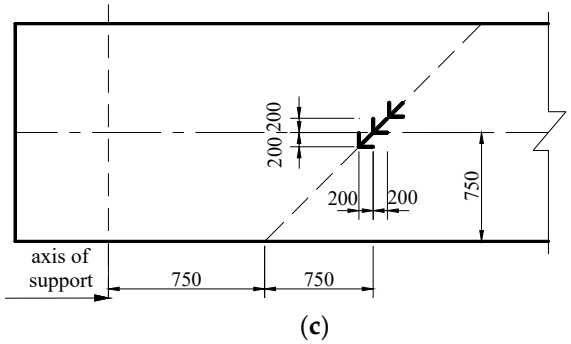

Figure 6. Layout of measuring points: (**a**) Schematic of testing Instrumentation (unit: mm); (**b**) detail of reinforcement strain measuring points; (**c**) schematic of rosette strain gauges.

(2) Rotation Measurement: Two dial gauges positioned horizontally were set at each end of the beam to measure the rotation angle of the beam at the fixed and movable hinge supports. There were four horizontal dial gauges, as shown in Figure 6a.

(3) Concrete Strain Measurement: The longitudinal strain of concrete was measured using resistance strain gauges (section A-A, B-B, C-C, D-D, and E-E). The strain gauges were attached on the surface of concrete along the longitudinal direction of the beam. There were three measuring points on the top side at each section, eight on the web, and three on the bottom. A total of 14 points was arranged at each section, and 80 points over the beam, as shown in Figure 6a.

(4) Reinforcement Strain Measurement: The reinforcement strain was determined by resistance strain gauge located on the corresponding position on section F-F, G-G, and H-H. There were seven outer longitudinal bars (N3) in the top and bottom slab. The measurement points were arranged on them longitudinally in the interval of one, as shown in Figure 6b. The number of strain measurement points of the bars in top slab was 4, as well as the bars in bottom slab. There were totally 24 measurement points for obtaining the strain of reinforcement.

(5) Measurement of Shear Strain: The principal tensile strains of concrete in the shear-bending zone were measured by three rosette strain gauges located on section I-I and section J-J, as detailed in Figure 6c. There were 12 rosette strain gauges on the test beam totally.

2.5. Loading Scheme

2.5.1. Fatigue Load

To avoid the resonance, the fatigue load was applied through electrohydraulic servo static and dynamic loading at a frequency of 2 Hz, while the natural frequency is calculated as 5.01 Hz. The upper and lower limit load in the fatigue were determined according to actual conditions. The lower limit load was related to the designed secondary dead load [31], and to apply the same bending moment to the midspan of the specimen, the lower limit load was calculated as:

$$\mathrm{P}_{\min} = q{l_0}^2/2(l_0 - l_M) = 39.97\mathrm{kN} \quad (1)$$

where q is the secondary dead load designed as 3 kN/m; l_0 is the net span; l_M is the distance between the two loading points.

Similar to the method of calculating the lower limit load, the upper limit of fatigue load is based on the most unfavorable combination of the maximum standard load (secondary dead load plus variable load considering impact factor). The variable load is calculated in the case of the train is fully loaded, that is, P = 120 kN, as shown in Figure 7. Considering a reduction coefficient as 0.9 provided by the architect, the upper limit is calculated as 348 kN. The design details of fatigue test are characterized in Table 4.

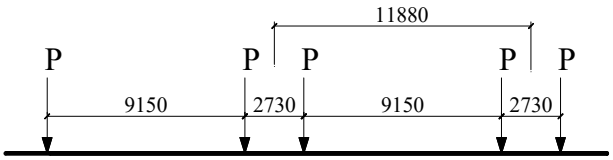

Figure 7. Schematic of monorail vehicle load (unit: mm).

Table 4. Test loading value.

Test	Fatigue Load		Post-Fatigue Static Load								
grade	min	max	1	2	3	4	5	6	7	8	9
Load (kN)	39.97	347.95	0	47.3	142.0	236.6	331.3	425.9	473.3	236.6	0

2.5.2. Post-Fatigue Static Load

During the fatigue loading test, the repeated loading was first periodically paused and the specimen was unloaded to zero when the fatigue cycle ranges to 0 time (before the test), 100,000 times, 500,000 times, 1,000,000 times, and every 1,000,000 times thereafter until 6,000,000 times. Then the dial gauges were placed, ensuring the pointers were in sufficient contact and zero the dial gauges [32]. Subsequently, the load was loaded sequentially from zero to the maximum static load Ps at the step shown in Table 4. At the interval time of each grade of post-fatigue static load and when digits of the dial gauges became steady, the deformation and strain information of the structure were monitored. The crack was observed in the web, top, and bottom slab throughout the test. The complete loading procedure of the test is shown in Figure 8.

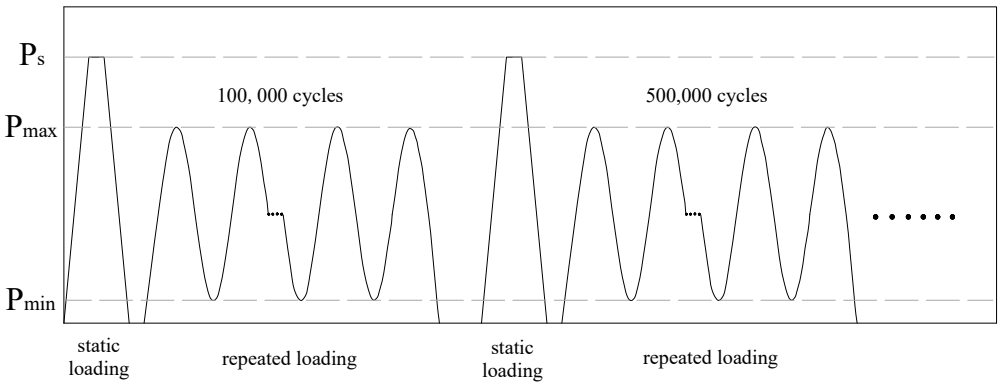

Figure 8. Procedure of the test.

Similar to the method in calculating the upper limit load, the maximum static load P_s is also obtained by the addition of the secondary dead load and variable load (considering impact factor), except that the variable load in this case is calculated as the train is overcrowding. That is, P is considered as 150 kN, which is shown in Figure 7; P_s is calculated as 473 kN.

3. Finite Element Model

The three-dimensional finite element model was established based on the commercial finite element program ANSYS. Concrete was simulated using a 3D eight-node solid element, namely SOLID 65. As shown in Figure 9, a model proposed by Hognestad [33] was applied to describe the compression constitutive relationship of concrete as follows:

Rising branch ($\varepsilon \leq \varepsilon_0$):

$$\sigma = f_c[2\frac{\varepsilon}{\varepsilon_0} - (\frac{\varepsilon}{\varepsilon_0})^2] \quad (2)$$

Falling branch ($\varepsilon_0 \leq \varepsilon \leq \varepsilon_u$):

$$\sigma = f_c[1 - 0.15\frac{\varepsilon - \varepsilon_0}{\varepsilon_u - \varepsilon_0}] \tag{3}$$

where f_c is the peak stress, i.e., prism compressive strength of concrete; ε_0 is the strain correspond to peak stress; ε_u is the ultimate compression strain of concrete.

The tensile constitutive relationship of the concrete was defined in two parts: the elastic part from zero to the ultimate value and the descending part determined by Equation (4).

$$\sigma_t = \frac{\rho_t}{\alpha_t(x_t - 1)^{1.7} + x_t} E_c \varepsilon_t \tag{4}$$

where $\rho_t = f_t/(E_c\varepsilon_{tr})$; σ_t and ε_0 are the tensile stress and tensile strain respectively; f_t is the tensile strength; $\varepsilon_{tr}(= 0.0001)$ is the strain when the σ_t reaches f_t; α_t is a parameter related to the shape of descending part of tensile constitutive relationship; $x_t = \varepsilon_t/\varepsilon_{tr}$ and $x_t > 1$ for the descending part.

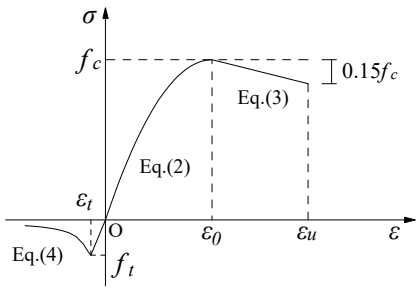

Figure 9. Constitutive relation of concrete.

The reinforcement and prestressed tendons were simulated using a 3D two-node link element, namely LINK 180, as shown in Figure 10a,b. The modulus of elasticity was regarded as constant. No relative slippage between concrete and reinforcement was considered, as well as prestressed tendons [34]. The prestressed forces in tendons were applied by defining an initial strain. Tendons had been united with the concrete by establishing reasonable constraint equations between tendons nodes and concrete nodes.

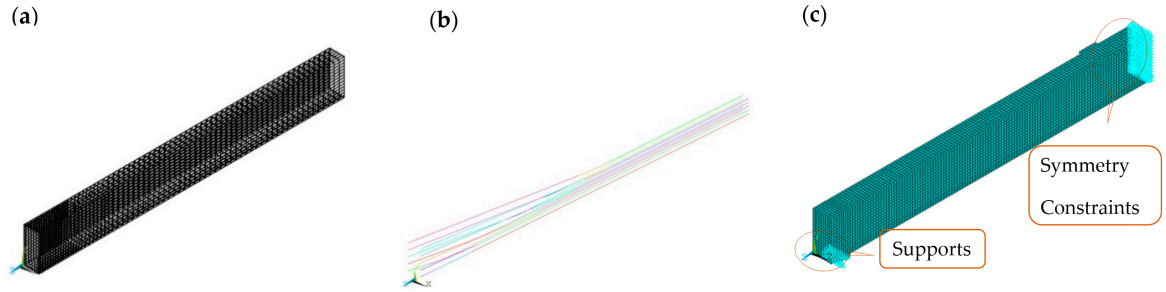

Figure 10. Finite element model based on the commercial finite element program ANSYS: (**a**) Reinforcement; (**b**) prestressed tendons; (**c**) 1/2 beam model.

Due to the symmetry of the specimen, only a half of the structure was modelled, with symmetric constraints on the midspan section, as shown in Figure 10c. A schematic of the symmetric constraints is shown in Figure 11.

The load applied through the electrohydraulic servo actuator was modeled as a knife edge load. To eliminate the effects of stress concentration, a rigidity block was modeled at the loading points as well as the support position.

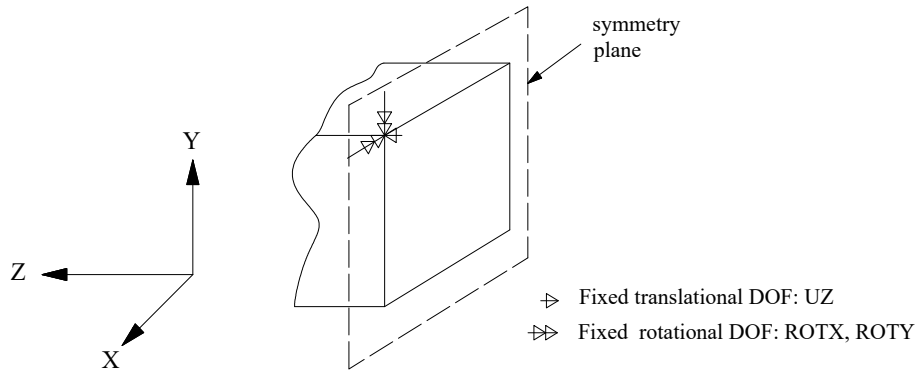

Figure 11. Schematic of symmetric constraints used in the midspan section.

4. Results and Discussions

4.1. Displacement and Stiffness

As shown in Figure 12, the displacement of section C-C at midspan approximately linearly increases with the applied load in a post-fatigue static load test, indicating that the beam behaves within its linearly elastic stage under the overcrowding load (Ps). Figure 13 shows the development of displacement at section B-B, C-C, and D-D, when the maximum static load was applied. The values range from 13.5 mm to 13.8 mm at section C-C (midspan), and from 8.9 mm to 9.3 mm at section B-B and D-D (quarter-span), which have been deducted from bearing settlement. Displacement at each section rarely changes in the test, indicating the good stiffness performance [35]. Thus, when analyzing the mechanical property of the structure in a fatigue test by finite element model, the change of the stiffness can be ignored. The result in finite element analysis is shown as dashed lines in Figure 13, which match well with the experiment result with a difference of 2.18% in mid-span and 6.36% in L/4 section. The difference is supposed to be due to the simplification of the model, for example, no relative slippage between concrete and reinforcement was considered [36], and the material constitutive equations were simplified as well. However, the difference is really small, so the finite element analysis model is considered to have been validated.

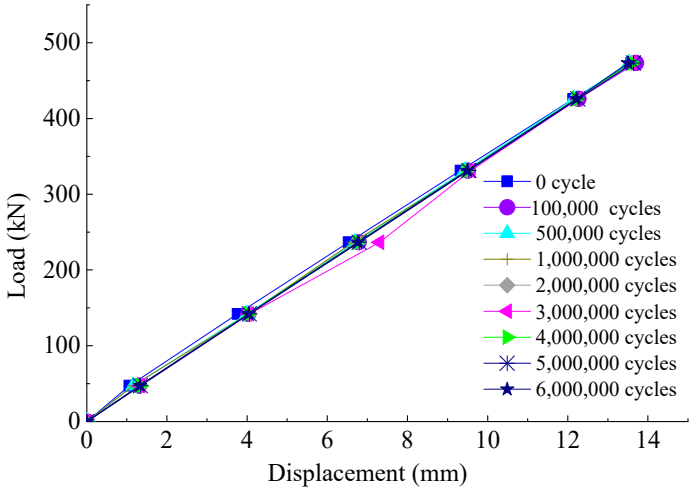

Figure 12. Static load-displacement curve at midspan.

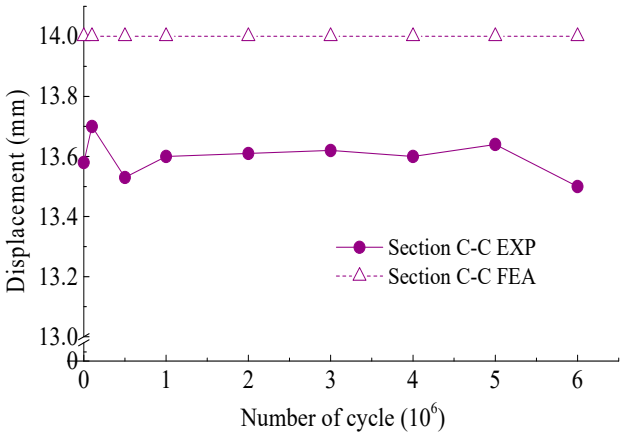

(**a**)

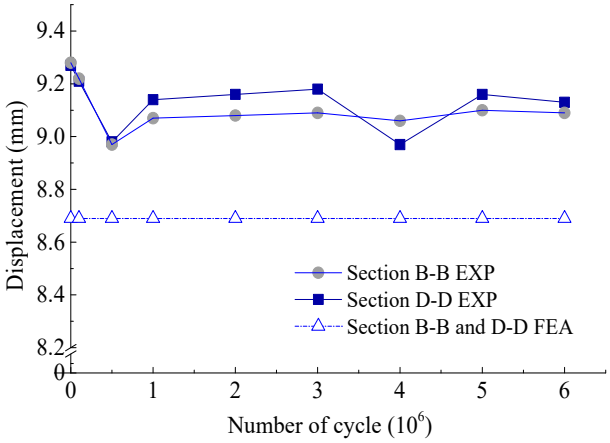

(**b**)

Figure 13. Displacement versus cycles: (**a**) section B-B and section D-D; (**b**) section C-C. "EXP" represents experimental result, and "FEA" represents finite element analysis result.

According to material mechanics, the diagrammatic multiplication method for calculating the deflection of a simple supported beam under the static load is as follows [37]:

$$f = \int \frac{\overline{M} M_P \mathrm{ds}}{B_s} \tag{5}$$

where $\overline{M}$ is the moment diagram of midspan when a unit force is applied; M_P is the moment diagram of midspan when the static load P_s is applied, and B_s is the bending stiffness of the beam.

The formula of the bending stiffness obtained from Equation (5) is shown in Equation (6):

$$B_s = \frac{\int \overline{M} M_P \mathrm{ds}}{f} \tag{6}$$

4.2. Rotation

As shown in Table 5, the rotation angle nearing the fixed hinge support ranged from 0.095° to 0.101° when the maximum static load was applied, while the angle nearing the movable supports ranged from 0.095° to 0.101°. Both of them are almost constant with slight fluctuation and have an

overall upward trend, which is related to the slight decrease of stiffness. They were found to have similar values under repeated loading, indicating the equivalent constraints of the two ends.

Table 5. The angle of the beam end.

Cycles (10^6)	0	10	50	100	200	300	400	500	600
Fixed (degrees)	0.099	0.099	0.098	0.101	0.099	0.101	0.101	0.100	0.101
Movable (degrees)	0.095	0.100	0.100	0.100	0.099	0.099	0.097	0.101	0.101

The Rotational Stiffness of the beam under the static load is calculated as follows:

$$R_s = \frac{M}{\theta} \tag{7}$$

where M is the maximum bending moment of the midspan section; θ is the rotation angle of the beam, and it is an average of the rotation angles of both ends of the beam in this study.

Finally, the variation of bending stiffness calculated from Equation (6) and rotational stiffness calculated from Equation (7) is shown in Table 6, and both of them were fluctuating slightly during the fatigue test, indicating the good performance of the specimen under repeated loads.

Table 6. The bending stiffness and rotational stiffness versus cycles.

Cycles (10^6)	0	10	50	100	200	300	400	500	600
Bending Stiffness (10^6 kN m)	17.69	17.53	17.75	17.66	17.65	17.63	17.66	17.61	17.79
Rotational Stiffness (10^6 kN m/rad)	2.82	2.75	2.76	2.72	2.76	2.73	2.76	2.72	2.71

4.3. Strain of Concrete

With the increase of the fatigue loading cycle, the development of concrete stain at midspan when the maximum static load was applied is shown in Figure 14. The strains measured at these measuring points are almost constant except for a slight fluctuation at 2,000,000 cycles, similarly as the other sections. Figure 15 shows the relationship between the applied load and concrete strain in compression and tensile concrete in a post-fatigue static load test. Curves have a good coincidence except for a slightly difference at 2,000,000 cycles. Both of the compressive and tensile strains are linear with the increase of static load. The maximum strain in compression zone is -213 με, while that in tensile zone is 208 με. The concrete strain of pre-camber was counted in, and the actual strain is much smaller. No crack was observed throughout the loading-unloading process and the concrete was in linear-elastic, which complies with the design intention of a fully prestressed concrete component.

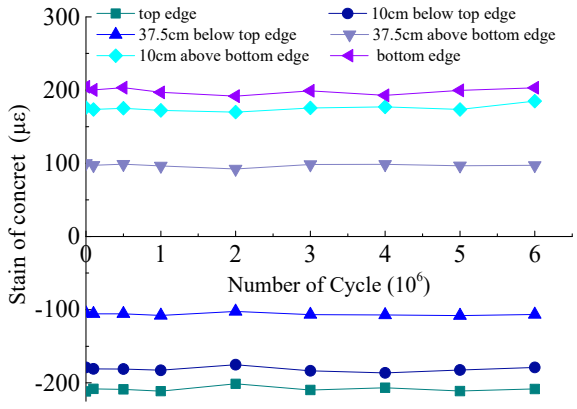

Figure 14. Concrete stain development at midspan.

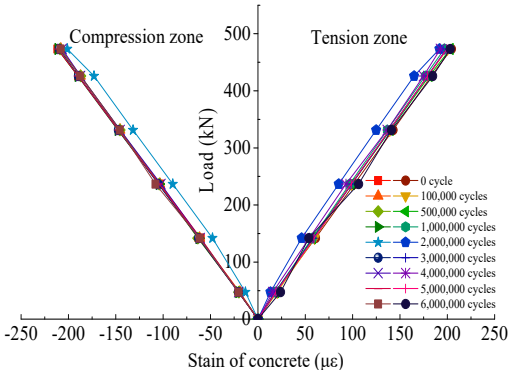

Figure 15. Load-concrete strain curves.

Crack is not allowed to occur in tensile concrete under service load (equal to P_{max}), and the concrete will remain linear-elastic under fatigue load (P_{min}~P_{max}) until the fatigue failure finally occurred in tensile reinforcement [38]. The specimen was conformed to the design intention and fabricated well. The arrangement of reinforcement improved the bond of concrete and prestressed tendons, reducing the stiffness degradation [13], which contributed the good mechanical characteristics under repeated loading [39,40].

Figure 16 shows the distributions of concrete strain at different measuring points when the maximum static load was applied. The distribution of each measuring point remains linear during the whole process of the test, which is consistent with the assumption of plane section [38].

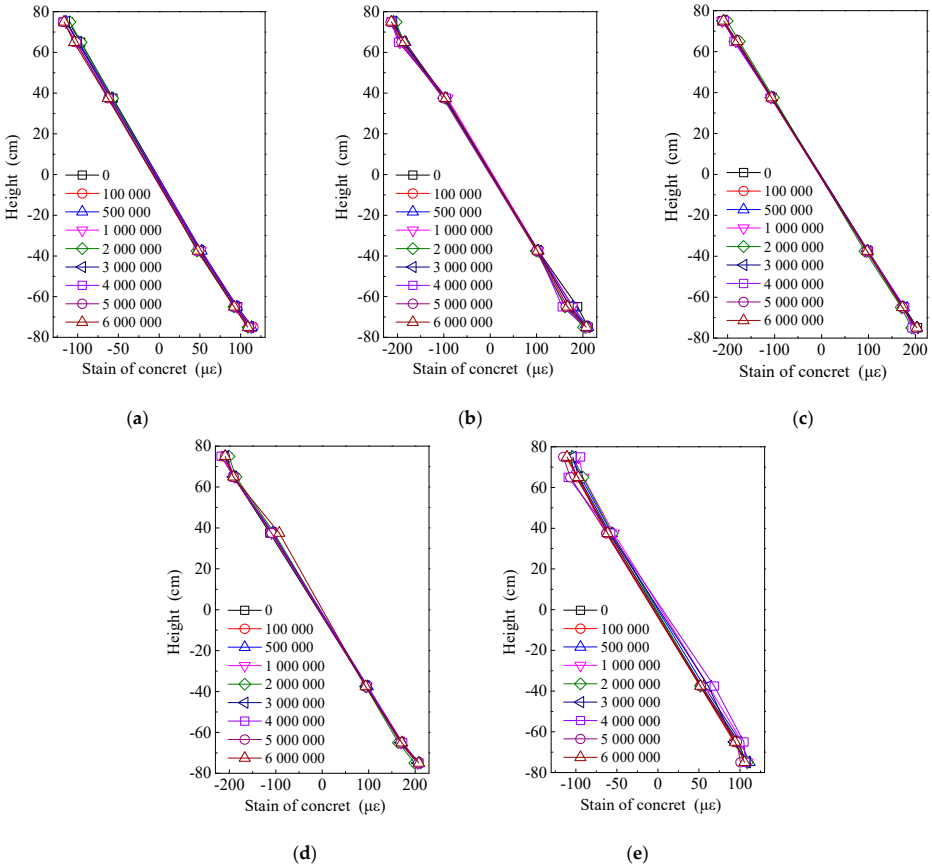

Figure 16. Distribution of concrete strain along height: (**a**) section A-A; (**b**) section B-B; (**c**) section C-C; (**d**) section D-D; (**e**) section E-E.

4.4. Strain of Reinforcement

The linear relationship between the strain of longitudinal reinforcement (N3) and applied load is shown in Figure 17. The maximum strain of the compression reinforcement is −207 με, while that of the tensile reinforcement is 191 με. The comparison between strains of reinforcement bar ε_{bar} and that of concrete at the same height as the bar $\varepsilon_{con,h-c}$ was shown in Table 7, where h is the height of specimen and c is the thickness of protection layer. The concrete strain was calculated using the assumption of plane section. The ratio of $\varepsilon_{con,h-c}$ to ε_{bar} ranges from 0.95 to 1.03, indicating that the deformation of concrete and steel is coordinated with each other and the bond between concrete and reinforcement was performing well throughout the test. The strain fluctuates slightly in the later period of the test, owing to the influence caused by the prestressed tendons that were closed to the reinforcement.

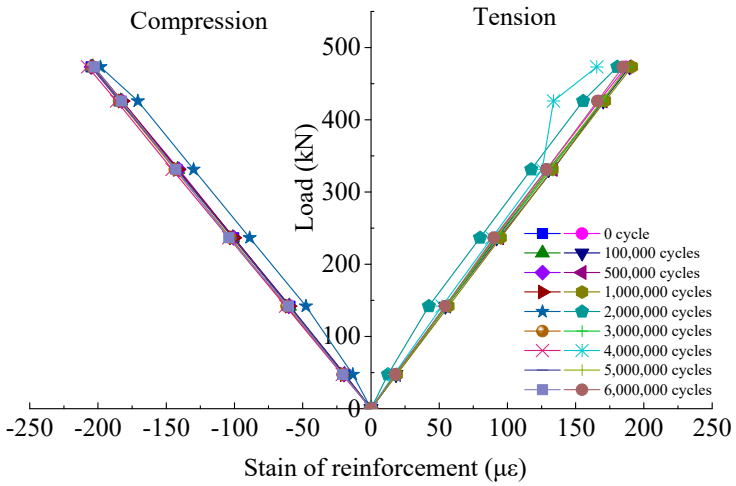

Figure 17. The relationship between the reinforcement strain and applied load.

Table 7. Relationship between reinforcement strain and concrete strain.

	Section B-B		**Section C-C**		**Section D-D**	
cycle	0	6,000,000	0	6,000,000	0	6,000,000
$\varepsilon_{con,h-c}$ (με)	196.6	181.0	185.96	182.82	182.34	184.19
ε_{bar}(με)	190.2	189.9	186.84	184.54	185.68	194.43
$\varepsilon_{con,h-c}/\varepsilon_{bar}$	1.03	0.95	0.99	0.99	0.98	0.95

The finite element analysis shows that the maximum tensile strain is 191 με, in the tensile reinforcement at midspan. The minimum compression strain is −212 με, in the compression reinforcement at midspan.

4.5. Shear Strain of Shear-Bending Zone

The linear relationship between the shear strain and applied load is shown in Figure 18. The value changed little in the post-fatigue static experiment after six million fatigue loading circles. There was a small difference in shear strain between the two sections, indicating the equivalent constraints of the two ends.

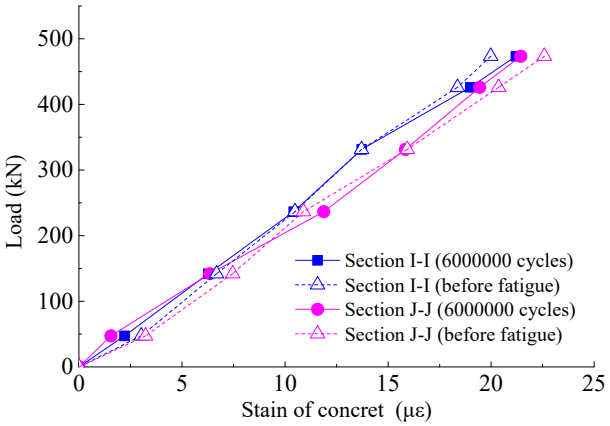

Figure 18. Load-shear strain curves.

5. Conclusions

Based on the above experimental investigations, conclusions can be drawn as follows:

- The PC track beam for monorail behaved within the linear-elastic stage when subjected to repeated service loadings with the upper and lower limit of 39.97 kN and 348 kN, respectively. The displacement of midspan slightly fluctuates between 13.5 mm and 13.8 mm, indicating the good stiffness performance of the beam. The displacement predicted using the 3D finite element model which ignored the change of the stiffness is reasonably accurate compared with the measured results.
- No crack was observed throughout the test, even after 6,000,000 cycles of repeated loading, indicating the good crack resistance of the beam. As a fully PC beam, the specimen was conformed to the design intention and fabricated well.
- The distribution of concrete strain remained linear during the whole process of the test, which is consistent with the assumption of plane section. The strain of reinforcement is a little different from that of concrete at the same height, and the ratio of the latter to the former ranges from 0.95 to 1.03, which indicates that the bond between concrete and reinforcement performed well throughout the test.

Author Contributions: Conceptualization, H.W. and H.G.; Methodology, Q.P. and H.W.; Software, H.W. and Y.B.; Validation, H.G. and Y.B.; Formal Analysis, H.W. and H.G.; Investigation, Q.P. and M.Y.; Resources, Q.P.; Data Curation, M.Y.; Writing-Original Draft Preparation, H.W.; Writing-Review & Editing, H.W. and H.G.; Visualization, H.W. and Y.B.; Supervision, H.G.; Project Administration, Q.P.; Funding Acquisition, Q.P.

Funding: The research described in this paper was financially supported by the National Natural Science Foundation of China (Grant Nos. 51508474 and 51108382), the Sichuan Science and Technology Program (Grant No. 2018JY0294), and the Science and Technology Research and Development Plan of China Railway Construction (Grant No. 2014-C34).

Conflicts of Interest: The authors declare no conflict of interest. The funders had no role in the design of the study; in the collection, analyses, or interpretation of data; in the writing of the manuscript, and in the decision to publish the results.

References

1. Wang, M.S. Development Orientation of Urban Transit in China. *J. Railw. Eng. Soc.* **2003**, *3*, 43–47. (In Chinese)
2. Liu, X.; Liu, P.; Wang, Q.; Long, L. Feasibility Analysis on Application of Modified Concrete Contains Rubber Powder of Straddle Type Monorail Train Waste Tire. *Procedia Environ. Sci.* **2016**, *31*, 804–811. [CrossRef]
3. Manoratna, D.A.; Kawata, K.; Yoshida, Y. Environmental Impact and Travel Time Savings of a New Monorail System in Colombo's Commuting Traffic. *Transp. Res. Part D Transp. Environ.* **2017**, *51*, 122–128. [CrossRef]

4. Kuwabara, T.; Hiraishi, M.; Goda, K.; Okamoto, S.; Ito, A.; Sugita, Y. New Solution for Urban Traffic: Small-type Monorail System. In Proceedings of the 10th International Conference on Automated People Movers, Orlando, FL, USA, 1–4 May 2005. [CrossRef]
5. Yildiz, A.S.; Sivrioglu, S. Semi-Active Vibration Control of Lateral and Rolling Motions for a Straddle Type Monorail Vehicle. *IFAC-Pap. Online* **2016**, *49*, 279–284. [CrossRef]
6. Zhong, M.L.; Zhu, E.Y. Development of Emergency Track Beam Alignment for Rapid Track Beam Replacement of Straddle Monorail Transit. *J. Transp. Eng.* **2013**, *139*, 416–423. [CrossRef]
7. Song, A.; Wan, S.; Jiang, Z.; Xu, J. Residual Deflection Analysis in Negative Moment Regions of Steel-Concrete Composite Beams under Fatigue Loading. *Constr. Build. Mater.* **2018**, *158*, 50–60. [CrossRef]
8. Hanson, J.M.; Hulsbos, C.L. Fatigue Tests of Two Prestressed Concrete I-Beams with Inclined Cracks. *Highw. Res. Rec.* **1965**, *103*, 14–30.
9. Yuan, M.; Yan, D.; Zhong, H.; Liu, Y. Experimental Investigation of High-Cycle Fatigue Behavior for Prestressed Concrete Box-Girders. *Constr. Build. Mater.* **2017**, *157*, 424–437. [CrossRef]
10. Muller, J.F.; Dux, P.F. Fatigue of Prestressed Concrete Beams with Inclined Strands. *J. Struct. Eng.* **1994**, *120*, 1122–1139. [CrossRef]
11. Brenkus, N.R.; Wagner, D.J.; Hamilton, H.R. Experimental Evaluation of Flexural Static and Fatigue Strength of an Innovative Splice for Prestressed Precast Concrete Girders. *J. Bridge Eng.* **2016**, *21*, 04016017. [CrossRef]
12. Rosenboom, O.; Rizkalla, S. Behavior of Prestressed Concrete Strengthened with Various CFRP Systems Subjected to Fatigue Loading. *J. Compos. Constr.* **2006**, *10*, 492–502. [CrossRef]
13. Haraj1i, M.H.; Naaman, A.E. Static and Fatigue Tests on Partially Prestressed Beams. *J. Struct. Eng.* **1985**, *111*, 1602–1618. [CrossRef]
14. Feng, X.; Song, Y.; Zhang, J.; Xiuhua, Q.U. Experimental Study on Stress Redistribution of Reinforcing Steel in Prestressed Concrete Beams under Fatigue Loading. *J. Build. Struct.* **2006**, *27*, 94–99. (In Chinese)
15. Wollmann, G.P. Fretting Fatigue in Post-Tensioned Concrete Beams. *Aci Struct. J.* **1996**, *93*, 171.
16. Li, J.Z.; Yu, Z.W.; Li, S. Stiffness degradation regularity of PC beam under fatigue repeated loading. *J. Highw. Transp. Res. Dev.* **2013**, *30*, 62–69.
17. Naaman, A.E.; Founas, M. Partially prestressed beams under random-amplitude fatigue loading. *J. Struct. Eng.* **1991**, *117*, 3742–3761. [CrossRef]
18. Saiedi, R.; Green, M.F.; Fam, A. Behavior of CFRP-Prestressed Concrete Beams under Sustained Load at Low Temperature. *J. Cold Reg. Eng.* **2013**, *27*, 1–15. [CrossRef]
19. Saiedi, R.; Fam, A.; Green, M.F. Behavior of CFRP-Prestressed Concrete Beams under High-Cycle Fatigue at Low Temperature. *J. Compos. Constr.* **2011**, *15*, 482–489. [CrossRef]
20. Huang, H.; Wang, W.W.; Dai, J.G.; Brigham, J.C. Fatigue behavior of reinforced concrete beams strengthened with externally bonded prestressed CFRP sheets. *J. Compos. Constr.* **2016**, *21*, 04016108. [CrossRef]
21. Ye, H.W.; Li, C.J.; Pei, S.L.; Ummenhofer, T. Fatigue performance analysis of damaged steel beams strengthened with prestressed unbonded CFRP plates. *J. Bridge Eng.* **2018**, *23*, 04018040. [CrossRef]
22. Gou, H.; Zhou, W.; Bao, Y.; Li, X.; Pu, Q. Experimental Study on Dynamic Effects of a Long-span Railway Continuous Beam Bridge. *Appl. Sci.* **2018**, *8*, 669. [CrossRef]
23. Gou, H.; Zhou, W.; Yang, C.; Bao, Y.; Pu, Q. Dynamic response of long-span concrete-filled steel tube tied arch bridge and riding comfort of monorail trains. *Appl. Sci.* **2018**, *8*, 650. [CrossRef]
24. Gou, H.Y.; He, Y.N.; Zhou, W.; Bao, Y.; Chen, G.D. Experimental and numerical investigations of the dynamic responses of an asymmetrical arch railway bridge. *Proc. Inst. Mech. Eng. Part F J. Rail Rapid Transit* **2018**. [CrossRef]
25. Gou, H.Y.; Zhou, W.; Chen, G.D.; Bao, Y.; Pu, Q.H. In-situ test and dynamic analysis of a double-deck tied-arch bridge. *Steel Compos. Struct.* **2018**, *27*, 161–175.
26. Gou, H.Y.; Long, H.; Bao, Y.; Chen, G.D.; Pu, Q.H.; Kang, R. Experimental and numerical studies on stress distributions in girder-arch-pier connections of long-span continuous rigid frame arch railway bridge. *J. Bridge Eng.* **2018**, *23*, 04018039. [CrossRef]
27. Gou, H.Y.; Wang, W.; Shi, X.Y.; Pu, Q.H.; Kang, R. Behavior of steel-concrete composite cable anchorage system. *Steel Compos. Struct.* **2018**, *26*, 115–123.
28. Gou, H.Y.; Shi, X.Y.; Zhou, W.; Cui, K.; Pu, Q.H. Dynamic performance of continuous railway bridges: Numerical analyses and field tests. *Proc. Inst. Mech. Eng. Part F J. Rail Rapid Transit* **2018**, *232*, 936–955. [CrossRef]

29. Cui, C.; Zhang, Q.; Luo, Y.; Hao, H.; Li, J. Fatigue reliability evaluation of deck-to-rib welded joints in osd considering stochastic traffic load and welding residual stress. *Int. J. Fatigue* **2018**, *111*, 151–160. [CrossRef]
30. Zhang, Q.; Liu, Y.; Bao, Y.; Jia, D.; Bu, Y.; Li, Q. Fatigue performance of orthotropic steel-concrete composite deck with large-size longitudinal trough. *Eng. Struct.* **2017**, *150*, 864–874. [CrossRef]
31. Chen, Z.; Cao, H.; Ye, K.; Zhu, H.; Li, S. Improved particle swarm optimization-based form-finding method for suspension bridge installation analysis. *J. Comput. Civil. Eng.* **2015**, *9*, 04014047. [CrossRef]
32. Liu, F.; Zhou, J.; Yan, L. Study of stiffness and bearing capacity degradation of reinforced concrete beams under constant-amplitude fatigue. *PLoS ONE* **2018**, *13*, e0192797. [CrossRef] [PubMed]
33. Hognestad, E. *Study of Combined Bending and Axial Load in Reinforced Concrete Members*; University of Illinois at Urbana Champaign: Champaign, IL, USA, 1951.
34. Li, X.; Bao, Y.; Xue, N.; Chen, G. Bond strength of steel bars embedded in high-performance fiber-reinforced cementitious composite before and after exposure to elevated temperatures. *Fire Saf. J.* **2017**, *92*, 98–106. [CrossRef]
35. Linaresunamunzaga, A.; Gonzaloorden, H.; Minguela, J.; Pérezacebo, H. New Procedure for Compacting Prismatic Specimens of Cement-Treated Base Materials. *Appl. Sci.* **2018**, *8*, 970. [CrossRef]
36. Neto, P.; Alfaiate, J.; Vinagre, J. Numerical modelling of concrete beams reinforced with pre-stressed CFRP. *Key Eng. Mater.* **2007**, *348–349*, 685–688. [CrossRef]
37. Long, Y.Q. *Structural Mechanics*; Higher Education Press: Beijing, China, 2002.
38. Fauchart, J.; Kavyrchine, M.; Trinh, J. Left bracket performance of prestressed and reinforced concrete joists under repeated loads right bracket. *Ann. 1' Inst. Tech. Batiment Trav. Publics* **1975**, *326*, 21–31.
39. Abeles, P.W.; Brown, E.L.; Hu, C.H. Behavior of under-reinforced prestressed concrete beams subjected to different stress ranges. *ACI* **1974**, *SP41-12*, 237–277.
40. Sun, W.W.; Wei, F. Numerical investigation of the effects of connection rotational stiffness on block shear capacity of coped beams with a welded end connection. *Int. J. Steel Struct.* **2011**, *11*, 325. [CrossRef]